

## In-medium properties of mesons

Volker Metag<sup>1,2,\*</sup>, Mariana Nanova<sup>1,\*\*</sup>, and Kai-Thomas Brinkmann<sup>1,\*\*\*</sup>

<sup>1</sup>II. Physikalisches Institut, Universität Gießen, Germany

<sup>2</sup>Helmholtz Institut für Strahlen- und Kernphysik, Universität Bonn, Germany

**Abstract.** In the project **B.4**, the modification of meson properties (mass, width) in a nuclear medium has been studied in photoproduction of mesons off nuclear targets. This work has been motivated by theoretical expectations of in-medium modifications of hadrons based on the conjecture of a partial restoration of chiral symmetry in a strongly interacting medium. It has been shown that these in-medium changes can be discussed in a compact form in terms of an optical potential describing the meson-nucleus interaction. Experimental approaches to determine the real and imaginary part of the meson-nucleus potential have been developed. The experiments have been performed with the Crystal Barrel/TAPS detector at the electron accelerator ELSA (Bonn) and the Crystal Ball/TAPS detector at MAMI (Mainz). Measuring the excitation function and momentum distribution for photo production of  $\omega$  and  $\eta'$  mesons, the real parts of the  $\omega$  and  $\eta'$ -nucleus potential, given by the in-medium mass shift, have been determined. For the  $\eta'$  meson a lowering of the mass at normal nuclear matter density by  $-(39 \pm 7(\text{stat}) \pm 15(\text{syst}))$  MeV is observed, while for the  $\omega$  meson a slightly smaller mass shift is found, however, with much larger uncertainties, not excluding a zero mass shift. The imaginary part of the potentials has been extracted from the measurement of the transparency ratio which compares the meson production cross section per nucleon within a nucleus to the production cross section off the free proton. For the  $\eta'$  meson the imaginary part of the potential is found to be smaller than the real part. In case of the  $\omega$  meson the opposite is observed. This makes the  $\eta'$  meson a good candidate for the search for meson-nucleus bound states while no resolved  $\omega$  mesic states can be expected. The results are compared with theoretical predictions. An outlook on future experiments is given.

## 1 Introduction

The interaction of mesons with nuclei is an important testing ground for our understanding of Quantum Chromodynamics (QCD) as the theory of the strong interaction in the non-perturbative regime. Research in this field was motivated in particular by theoretical predictions that meson properties might change within nuclei due to a partial restoration of chiral symmetry [1–3]. Mesons are considered to be excitations of the QCD vacuum which has a complicated structure with non-vanishing chiral-, gluon- and higher order quark-condensates. These condensates are predicted to change within a strongly interacting medium and, as a consequence, also the excitation energy spectrum, i.e. the mass spectrum of mesons is expected to be modified. This idea fostered widespread theoretical and experimental activities which have been summarized in recent reviews [4–6].

Pseudoscalar mesons are particularly suited for studying in-medium modifications, as shown in Fig. 1 [7]. Spontaneous chiral symmetry breaking generates a pseudo scalar nonet ( $\pi, K, \bar{K}, \eta, \eta'$ ) of massless Goldstone bosons. The explicit breaking of the  $U(1)_A$  symmetry selectively

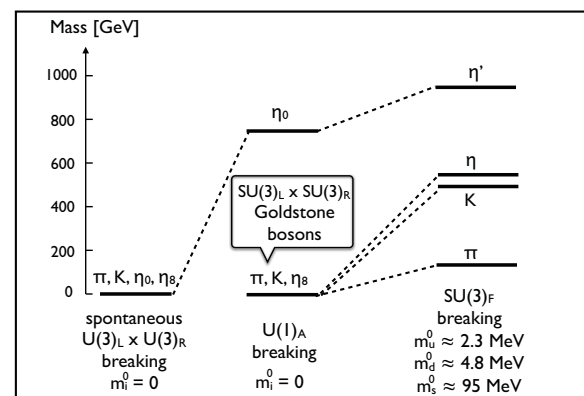


**Figure 1.** Symmetry breaking pattern for pseudoscalar mesons as described in the text, adapted from [7].

shifts up the  $\eta'$  mass, leaving the SU(3) flavor octet of pions, kaons and  $\eta$  massless. Explicit chiral symmetry breaking by introducing non-zero quark masses then leads to the experimentally observed meson masses [1, 7, 8]. Since symmetry breaking has such a big effect on meson masses one would expect corresponding effects in case of

\* e-mail: volker.metag@exp2.physik.uni-giessen.de  
 \*\* e-mail: mariana.nanova@exp2.physik.uni-giessen.de  
 \*\*\* e-mail: kai-thomas.brinkmann@exp2.physik.uni-giessen.de

a partial restoration of this symmetry in a strongly interacting medium.

If spontaneously broken chiral symmetry were restored at high nuclear densities one would expect masses of vector mesons with spin parity  $J^\pi = 1^-$  to become degenerate in mass with their chiral partners with the same spin but opposite parity, the axial vector mesons with  $J^\pi = 1^+$ . Traces of this tendency should already show up at normal nuclear matter density and should thus become observable in photonuclear experiments

Many theory groups, using QCD-sum rules[3, 9] as well as various hadronic models such as the Nambu-Jona-Lasinio (NJL)-model [1, 10–13], the linear sigma model [14], the quark-meson-coupling model [15, 16], and coupled channel resonance models [17, 18] have made quantitative, but partially conflicting predictions for changes in mass and width of mesons in nuclei. As an example for the many calculations, the results obtained for the  $\eta'$  meson by Nagahiro et al. and for the  $\omega$  meson by Mühlich et al. are shown in Fig. 2 and Fig 3, respectively. Nagahiro et al.[11], applying the NJL model, predict a mass drop by  $\approx 150$  MeV for the  $\eta'$  meson at normal nuclear matter density. Within the coupled channel resonance model, Mühlich et al.[18] find a strong broadening but almost no mass shift for the  $\omega$  meson at saturation density. The broad range of predictions is summarized in table 1 for the  $\eta'$  meson and in table 2 for the  $\omega$  meson, respectively. This spread in theoretical predictions calls for an experimental clarification.

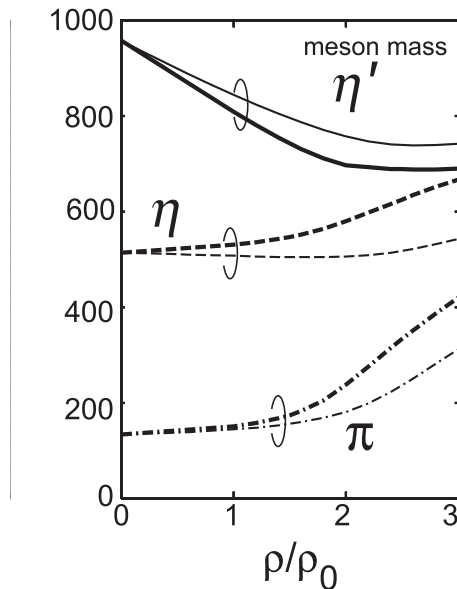


**Figure 2.** Meson masses calculated within the NJL model as function of the nuclear density  $\rho$ , normalized to the normal nuclear density  $\rho_0$ , for SU(2) symmetric matter (thick curves) and SU(3) symmetric matter (thin curves) [11].

It should be noted that most of these theoretical predictions have been calculated under idealized assumptions,

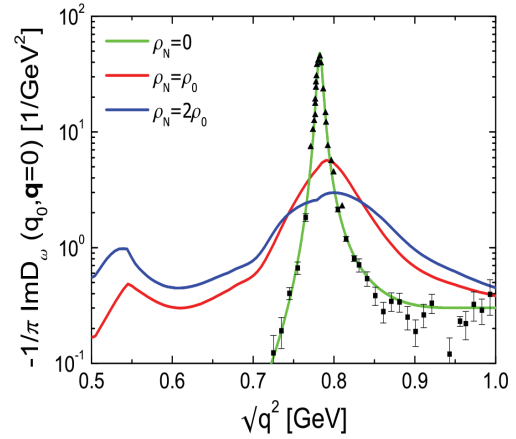


**Figure 3.** The spectral function for an  $\omega$  at rest, calculated within the coupled-channel resonance model for normal nuclear matter density  $\rho = \rho_0$  (solid curve) and for  $\rho = 2\rho_0$  (dashed curve) in comparison to the spectral function of a free  $\omega$  meson (dotted) [18].

**Table 1.** predictions for mass modifications of the  $\eta'$  meson at normal nuclear matter density.

model	ref.	$\Delta m (\rho = \rho_0)$
NJL	[10]	$\approx 0$ MeV/c <sup>2</sup>
NJL	[11]	$\approx -150$ MeV/c <sup>2</sup>
lin $\sigma$	[14]	$\approx -80$ MeV/c <sup>2</sup>
QMC	[16]	$\approx -40$ MeV/c <sup>2</sup>

**Table 2.** predictions for mass modifications of the  $\omega$  meson at normal nuclear matter density.

model	ref.	$\Delta m (\rho = \rho_0)$	$\Gamma (\rho = \rho_0)$
NJL	[1]	$\approx 0$ MeV/c <sup>2</sup>	
QCD SR	[3]	$\approx -120$ MeV/c <sup>2</sup>	
$L_{eff}$	[13]	$\approx -(100-150)$ MeV/c <sup>2</sup>	$\approx 40$ MeV
res. coupl.	[17]	$\approx -50$ MeV/c <sup>2</sup>	$\approx 40$ MeV
res. coupl.	[18]	$\approx 0$ MeV/c <sup>2</sup>	$\approx 60$ MeV
$\chi$ unitary	[19]		100-200 MeV
many-body	[20]		150-200 MeV

e.g. for a meson at rest in infinitely extended nuclear matter with constant density, a scenario far from reality. In photoproduction experiments in the 1-3 GeV energy range, the kinematics of the reaction leads to meson recoil momenta on average comparable to their mass; on the way out of the nucleus mesons see the nuclear density profile with a fall-off at the surface. Any density dependent mass shift or broadening is thereby smeared out due to the variation in density. A link between the theoretical predictions and the experimental observables is provided by transport calculations like, e.g. GiBUU [21]. These calculations take nuclear many-body effects into account which evolve dynamically in the course of the reaction. In particular they treat

- initial state effects: the absorption of incoming beam particles
- non equilibrium effects: varying density and temperature
- absorption and regeneration of mesons
- fraction of decays outside of the nucleus

- final state interactions: distortion of momenta of decay products.

It is indispensable to investigate with transport calculations how the above mentioned effects change the theoretically predicted initial signals before a meaningful comparison with experimental data can be performed to extract medium modifications of hadrons.

For long-lived mesons such as pions or kaons, meson beams can be used to study the meson-nucleus interaction experimentally. This is not possible for short-lived mesons like  $\eta$ ,  $\omega$ , and  $\eta'$  mesons where such beams are not available. Here, one has to produce the mesons in a nuclear reaction and to study their interaction with nucleons or nuclei in the final state. The meson-nucleus interaction and the in-medium modifications of mesons can be described by an optical potential

$$U(r) = V(r) + iW(r), \quad (1)$$

comprising a real ( $V(r)$ ) and an imaginary ( $W(r)$ ) part [11];  $r$  is the distance between the meson and the centre of the nucleus. In this presentation we discuss the determination of the real and imaginary part of the  $\omega$ - and  $\eta'$ - nucleus potential in photo production experiments off nuclei.

## 2 Experimental approaches to study mesons in the medium

The strength of the real part of the meson-nucleus potential is connected to the meson in-medium mass shift  $\Delta m(\rho_0)$  at saturation density  $\rho_0$  [11]

$$V(r) = \Delta m(\rho_0) \cdot c^2 \cdot \frac{\rho(r)}{\rho_0}. \quad (2)$$

The imaginary part of the potential describes the meson absorption in the medium via inelastic channels and is related to the in-medium width  $\Gamma_0$  of the meson at nuclear saturation density by [22]

$$W(r) = -\frac{1}{2}\Gamma_0 \cdot \frac{\rho(r)}{\rho_0}. \quad (3)$$

The experimental approaches to determine the real part of the potential listed below are applied for  $\omega$  and  $\eta'$  mesons and the results will be discussed later in this paper:

- line shape analysis
- excitation function of the meson
- momentum distribution
- meson-nucleus bound states

The theoretical predictions discussed in the introduction inspired many experiments searching for medium modifications like broadening, structures or mass shift. The experiments have focused on the light vector mesons  $\rho$ ,  $\omega$  and  $\phi$  with decay lengths comparable to nuclear dimensions. The mass distribution  $\mu(\vec{p}, \rho)$  depends on the 3-momentum  $\vec{p}$  of the vector meson and on the density  $\rho$  of the nuclear medium at the decay point. Only mesons decaying inside the nucleus carry information on in-medium properties which are to be studied. An in-medium mass

shift of the meson could be observed by comparing the mass calculated from Eq. (4) in the limit of low meson momenta with the vacuum mass of this meson listed in [23].

$$\mu(\vec{p}, \rho) = \sqrt{(p_1 + p_2)^2}. \quad (4)$$

The light vector mesons  $\rho$ ,  $\omega$  and  $\Phi$  are particularly suited for the mass distribution measurements since their lifetimes of 1.3 fm/c, 23 fm/c and 46 fm/c, respectively, are so short that they decay within the nuclear medium with some probability after production in a nuclear reaction. Nevertheless, momentum cuts have to be applied for the longer lived  $\omega$  and  $\Phi$  mesons to achieve decay lengths comparable to nuclear dimensions. Obviously the line shape analysis is not applicable for  $\eta'$  meson in the medium since its decay length is much larger than nuclear dimensions. In case of mesons with long lifetime decaying outside of the nucleus this method is not applicable since the information gained is the vacuum spectral function. The experimental results on the line shape analysis from the B4 project will be presented and discussed in section 5.2.1.

Weil et al. [24] discussed the possibility to extract information on the in-medium meson mass and the real part of the meson-nucleus potential from a measurement of the excitation function and/or momentum distribution of mesons in the photo production off a nucleus. Due to a lowering of the meson mass in the medium the meson production threshold will decrease and the enlarged phase space will lead consequently to increasing the production cross section for a given incident beam energy as compared to a scenario without mass shift. The dropping of the meson mass in the medium also affects the momentum distribution of the produced meson in the final state. When a meson is produced with a lower mass, then its total energy is on average also reduced due to kinematics. In addition, mesons produced within the nuclear medium must regain their free mass upon leaving the nucleus. Thus, in case of an in-medium mass drop, this mass difference has to be compensated at the expense of their kinetic energy. GiBUU transport-model calculations [24] demonstrated that there will be a downward shift in the momentum distribution for near-threshold energies as compared to a scenario without mass shift. A mass shift can thus be indirectly inferred from a measurement of the excitation function as well as from the momentum distribution of the meson. This idea, initially worked out for  $\omega$  mesons [24], has independently been pursued on a quantitative level for  $\eta'$  mesons by E. Paryev [25]. The experimental results about the determination of the real part of  $\omega$  and  $\eta'$  mesons from excitation functions and momentum distributions will be presented and discussed in sections 5.2.2 and 5.2.3.

A necessary condition for the experimental observation of meson-nucleus bound states is that  $|V| \gg |W|$ . It is therefore important to study experimentally the relative strengths of the real and imaginary part of the meson-nucleus interaction for the meson of interest. Then by the observation of meson-nucleus bound states information about the real and imaginary part of the meson-nucleus optical potential can be gained. The search for  $\omega$ - and  $\eta'$ -

nucleus bound states will be discussed in section 6.

The experimental observable for the imaginary part of the meson-nucleus optical potential is the transparency ratio measurement. As a definition, the transparency ratio compares the meson production cross section off a nucleon within a nucleus with the one off the free nucleon [26]:

$$T_A^m = \frac{\sigma_{\gamma A \rightarrow mX}}{A \cdot \sigma_{\gamma N \rightarrow mX}}. \quad (5)$$

Here, the nucleus serves as a target and at the same time as an absorber. If nuclei were completely transparent to the mesons the transparency ratio would be unity, as long as secondary production processes can be ignored. The results on the imaginary part of the  $\omega$ - and  $\eta'$ -nucleus optical potential will be discussed in section 5.3.

### 3 Experimental setup

The data on  $\omega$  and  $\eta'$  photoproduction were taken in a series of experiments in 2003, 2007, 2009 and 2013/14 with the Crystal Barrel/TAPS detector system at the ELSA accelerator in Bonn and in 2007, 2008 with the Crystal Ball and TAPS detector system at MAMI-C in Mainz.

#### 3.1 CBELSA/TAPS Detector system

The electron stretcher facility ELSA [27, 28] provides electrons with energy  $E_0$  which hit a primary radiation target, a thin copper or diamond crystal, and produce bremsstrahlung [29]. The energy of the bremsstrahlung photons is determined eventwise from the deflection of the scattered electrons in a magnetic field. From the energy of the scattered electron  $E_e^-$  the energy of the photon impinging on the nuclear target is given by  $E_\gamma = E_0 - E_e^-$ . Photons were tagged in the energy range from 0.5 GeV up to 3.1 GeV for an incoming electron energy of 3.2 GeV. The total tagged photon intensity was about  $10^7 \text{ s}^{-1}$  in this energy range. The part of the electron beam that did not produce any bremsstrahlung photons was deflected by the magnet as well. Since these electrons retained their full energy the curvature of their track is smaller and they passed over the tagger into a beam dump.

The Crystal Barrel and TAPS detector system at ELSA accelerator in Bonn used for data taking in 2003 is shown in Fig. 4 (left). The Crystal Barrel (CB) detector, a photon calorimeter consisting of 1290 CsI(Tl) crystals ( $\approx 16$  radiation lengths), covered the complete azimuthal angle and the polar angle from  $30^\circ$  to  $168^\circ$  [30]. The scintillating fibre-detector, surrounding the target in the center of the CB, was used to register charged particles [31]. The CB was combined with a forward detector - the TAPS calorimeter - consisting of 528 hexagonal BaF<sub>2</sub> crystals ( $\approx 12 X_0$ ), covering polar angles between  $5^\circ$  and  $30^\circ$  and the complete azimuthal angle [32, 33]. In front of each BaF<sub>2</sub> module a 5 mm thick plastic scintillator was mounted for the identification of charged particles.

The CB and TAPS detector system at ELSA used for data taking in 2007, 2009, 2013 and 2014, shown in Fig. 4 (right) is a new updated version of the first setup (Fig. 4

(left)). The main difference is the smaller TAPS detector (MiniTAPS), consisting of 216 BaF<sub>2</sub> modules, covering the angular range in the forward direction of  $1^\circ$  to  $11^\circ$ . In the range of  $11^\circ$ - $28^\circ$  the CsI(Tl) modules from CB (Forward Plug FP) were read out by photomultipliers, providing energy and time information while the rest of the CB crystals were read out by photodiodes with energy information only. A more detailed description of the detector setups and the running conditions can be found in [34–38].

Because of the high granularity and the large solid angle coverage of  $\approx 96\%$ , both detector system versions were ideally suited for the detection and reconstruction of multi-photon events.

Solid targets of  $^{12}\text{C}$ ,  $^{40}\text{Ca}$ ,  $^{93}\text{Nb}$  and  $^{208}\text{Pb}$ , used in the experiments, were mounted in the center of the CB.

#### 3.2 CB/TAPS@MAMI

In a series of experiments with tagged photon beams at MAMI-C, using the Crystal Ball and TAPS detector systems (Fig. 5),  $\omega$  photoproduction on  $^{12}\text{C}$  and  $^{93}\text{Nb}$  targets has been measured in the energy range close to the production threshold 900-1300 MeV [39]. The Crystal Ball detector, comprising 672 NaI(Tl) crystals with  $15.7 X_0$ , covered the polar angle range from  $20^\circ$  to  $160^\circ$ . The forward region was subtended by the TAPS calorimeter in a forward wall configuration, consisting of 384 BaF<sub>2</sub> crystals. The two innermost rings were replaced by 24 PbWO<sub>4</sub> ( $\approx 22 X_0$ ) crystals to handle higher event rates.

For the charged particle identification 5mm thick plastic scintillators, mounted in front of the BaF<sub>2</sub> crystals, were used. The particle identification detector (PID) surrounded the target area in the center of the Crystal Ball and consisted of 24 plastic scintillators. The MWPCs shown in Fig. 5 were not used in the experiments with solid targets. The combination of these detector systems was as suited for the detection of multi-photon final states as the CBELSA/TAPS detector.

### 4 Data analysis

The high segmentation and the almost full solid angle coverage of the detector systems used allowed the reconstruction of  $\omega$  and  $\eta'$  mesons from multi photon final states by invariant mass analysis. The decay modes used in the analyses were  $\omega \rightarrow \pi^0\gamma \rightarrow 3\gamma$  and  $\eta' \rightarrow \pi^0\pi^0\eta \rightarrow 6\gamma$  with branching ratios of 8.2% and 8.5%, respectively [23].

For the  $\omega$  analysis, events with exactly three photons and one charged hit in the detector system were selected. The invariant mass of all photon pairs was calculated and the one combination closest to the  $\pi^0$  mass of  $135 \text{ MeV}/c^2$  was taken to be the  $\pi^0$ . For the  $\eta'$  analysis, events with exactly 6 photons and any number of charged hits and with an energy sum of neutral clusters larger than 600 MeV were selected. The 6 photons were combined in 2 pairs of 2 photons with invariant masses in the range  $115 \text{ MeV}/c^2 \leq m_{\gamma\gamma} \leq 155 \text{ MeV}/c^2$  (corresponding to a

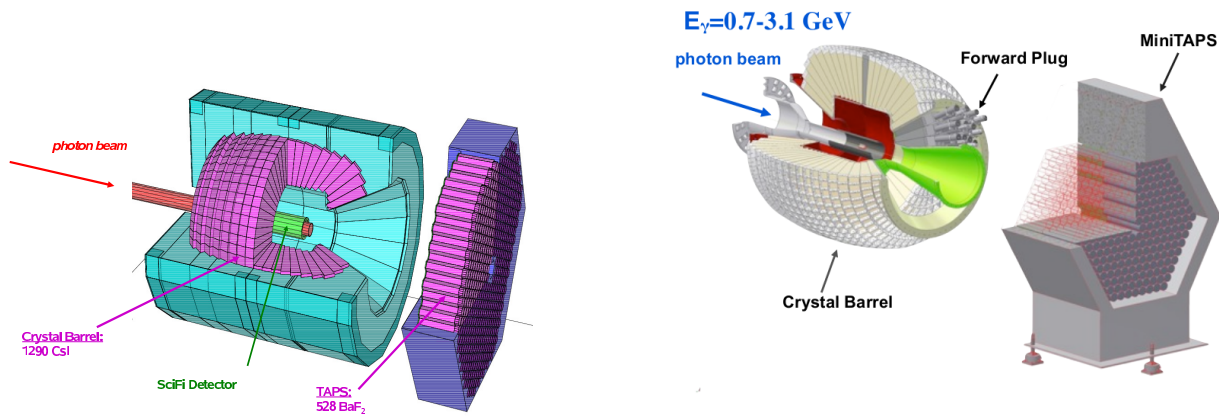


**Figure 4.** Left: Setup used in the experiment in 2003. Right: Improved setup used in the experiments with  $^{12}\text{C}$  (2007, 2009) and  $^{93}\text{Nb}$  (2013/14) targets. See text for more details.

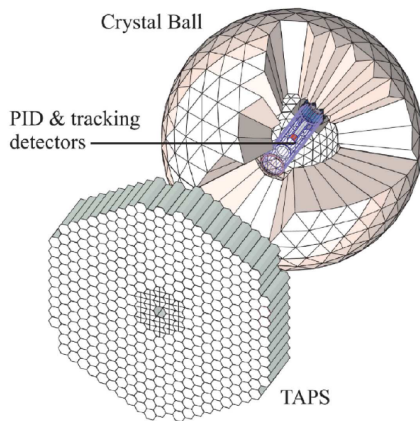


**Figure 5.** Crystal Ball/TAPS setup at MAMI in Mainz. Around the target area in the center of the Crystal Ball the plastic scintillator array (PID) and the multi-wire proportional chamber (MWPC) are shown. The  $\text{BaF}_2$  calorimeter TAPS in a forward wall configuration, subdivided into six sectors, with  $\text{PbWO}_4$  crystals in the two innermost rings, was placed in a distance of 1.47 m behind the target.

$\pm 3\sigma$  cut around  $m_{\pi^0}$ ) and one pair with invariant mass in the range  $510 \text{ MeV}/c^2 \leq m_{\gamma\gamma} \leq 590 \text{ MeV}/c^2$  (roughly corresponding to a  $\pm 2\sigma$  cut around  $m_\eta$ ). The best photon combination was selected based on a  $\chi^2$  minimization. To suppress the background from  $\eta \rightarrow 3\pi^0$  decays and direct  $3\pi^0$  production, events with 3  $\gamma$  pairs with an invariant mass within the limits for the pion mass  $m_{\pi^0}$  given above were removed from the data set.

Examples for the invariant mass spectra, the obtained mass resolution and signal/background ratio are shown in Fig. 6 and Fig. 7. For the  $\omega$  meson the relative mass resolution  $\frac{\sigma_m}{m}$  is about 3.3%, while for the  $\eta'$  meson a relative mass resolution of 1.2% has been achieved. The better  $\eta'$  mass resolution is due to the fact that the nominal mass values [23] of the three mesons in the final state can be

used in the calculation of the invariant mass. The signal/background ratios are of the order of 1/2.2 for the  $\omega$  and 1/1.2 for the  $\eta'$  meson, respectively.

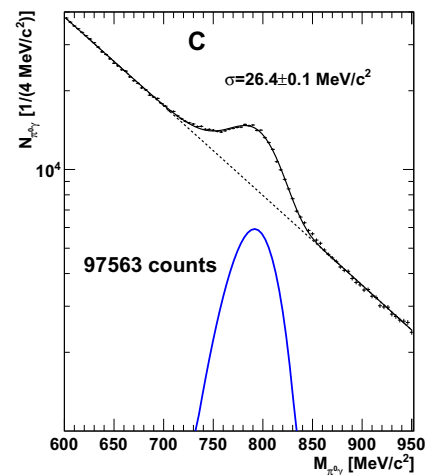


**Figure 6.**  $\pi^0\gamma$  invariant mass distribution measured for a carbon target [40].

The conversion of the observed meson yields into cross sections requires - apart from the incident photon flux - the knowledge of the meson reconstruction efficiency which is determined by Monte Carlo simulations. Applying the GEANT3 package [42] with a full implementation of the detector system, the nuclear reaction of interest is simulated, using as input the measured angular distributions of  $\omega$  and  $\eta'$  mesons produced off protons and neutrons bound in deuterium [43, 44]. In addition, the Fermi motion of nucleons in the target nucleus, as parameterized by [45], has been taken into account. The reconstruction efficiency is determined as a function of the laboratory angle and the momentum of the mesons. This approach ensures that the appropriate acceptance is used even if the angle

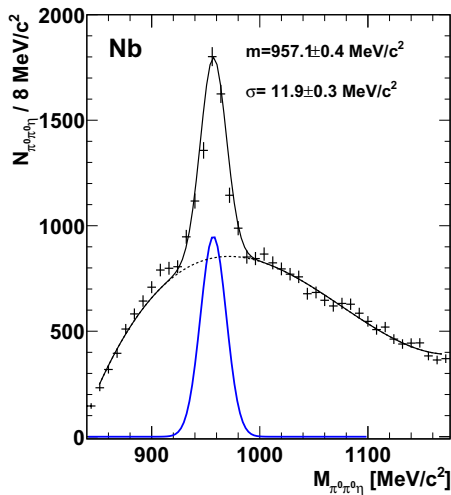


**Figure 7.**  $\pi^0\pi^0\eta$  mass distribution measured for a niobium target [41].

and momentum of the meson deviates from the kinematics of the reaction because of elastic scattering in the nucleus. The reconstruction efficiency is determined by taking the ratio of the number of reconstructed and the number of generated events for each angular- and momentum bin. As an example, the resulting reconstruction efficiency  $\epsilon_{\gamma\text{Nb} \rightarrow \eta'X}(p_{\eta'}^{\text{lab}}, \theta_{\eta'}^{\text{lab}})$  for the  $\gamma\text{Nb} \rightarrow \eta'X$  reaction is shown in Fig. 8 for the incident photon energy range of 1.2-2.9 GeV. In the Monte Carlo simulations, the same trigger conditions as in the experiment are applied.

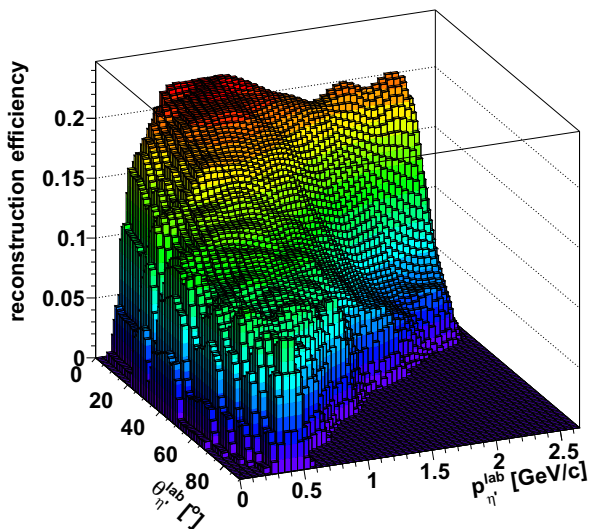


**Figure 8.** Two-dimensional reconstruction efficiency for  $\eta'$  photoproduction off Nb as a function of the  $\eta'$  momentum and angle in the laboratory system for the incident photon energy range of 1.2-2.9 GeV [41].

## 5 Results and discussion

### 5.1 Meson photoproduction in elementary reactions

Before extracting information on in-medium modifications of mesons from experiments, the photoproduction of mesons off the free proton as well as off the quasifree proton and neutron in deuterium has to be studied to provide a reference for the results obtained from nuclei. The photoproduction of  $\omega$  and  $\eta'$  mesons has been measured with the CBELSA/TAPS detector by Dietz et al. [43] and Jaegle et al. [44], respectively. Detailed results on the angular distributions and total cross sections have been obtained. As an example, the total cross section for  $\omega$  and  $\eta'$  production off the proton and neutron in deuterium are shown in Fig. 9. These data are essential as input for calculations of meson production off nuclei. Deviations from these calculations are then interpreted as in-medium effects.

### 5.2 The real part of the meson-nucleus optical potential

#### 5.2.1 Lineshape Analysis

As discussed in section 2, the most direct way to determine an in-medium mass shift from meson photoproduction off nuclear targets is to calculate the invariant mass from the measured 4-vectors of the meson decay products, using Eq. (4), and to compare this invariant mass with the meson mass listed in [23]. This approach has, however, several, disadvantages:

- The method is sensitive to the nuclear density at the *decay* point. Due to the kinematics of the reaction, mesons obtain a rather broad recoil momentum distribution with an average momentum comparable to their mass. Thus,  $\beta \cdot \gamma = \frac{p}{m} \approx 1$  and consequently, the average decay length  $\beta\gamma c\tau \approx c\tau$  is several times larger than nuclear dimensions even for short-lived vector mesons, except for the  $\rho$ . Most of the meson decays thus occur outside of the nuclear medium, yielding a free spectral function. Even when applying cuts to select low momentum mesons to enhance in-medium decays, there will always be two mass peaks for decays inside and outside of the nucleus which can only be separated if the mass shift is larger than the mass resolution.
- an in-medium mass peak will be smeared out depending on the broadening of the meson through inelastic reactions in the nucleus. Broad structures, however, will be more difficult to distinguish from background.
- ambiguities in the subtraction of the background in the invariant mass spectra leads to additional uncertainties in the determination of the meson line shape, as discussed in [36, 47, 49].
- the above problems exist for any decay mode of the meson. If, however, hadrons are among the decay products, as in the  $\omega$  and  $\eta'$  decays discussed here, the 4-momentum vectors of the decay products and thus also the calculated invariant mass may be distorted by elastic scattering or the mesons may even be absorbed within the nucleus due

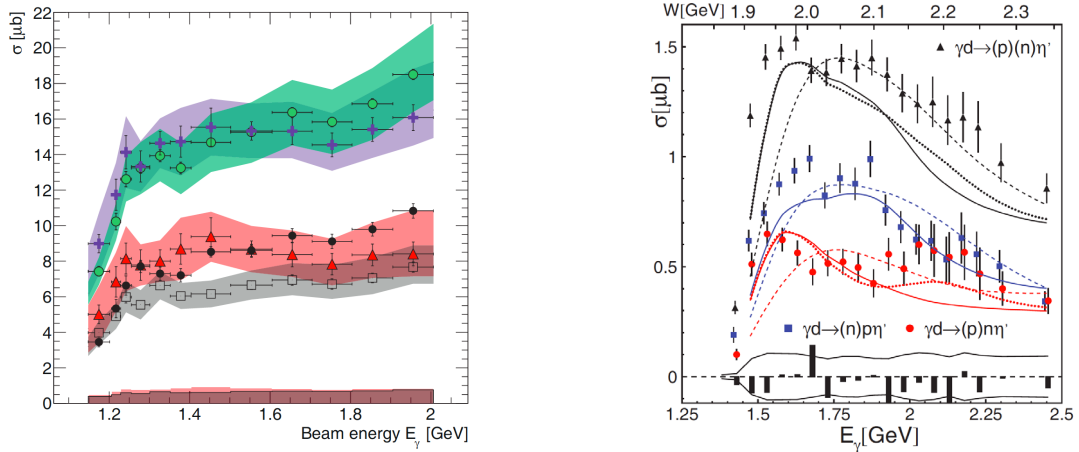


**Figure 9.** Left: Total cross section as a function of the incident photon energy for  $\omega$  mesons produced off the bound proton (open squares) and off the bound neutron (red triangles), the sum of the exclusive cross sections (purple crosses), the quasifree inclusive production cross section (green circles) and the cross section off the bound neutron calculated from  $\sigma_{incl} - \sigma_p^{bound}$  (black circles). The bands indicate the systematic errors [43]. Right: Total cross section as a function of the incident photon energy for  $\eta'$  production off the bound proton (blue squares) and neutron (red circles) and the inclusive cross section (black triangles). The curves are reaction model fits, see [44].

to the strong interaction. Information on decays near the center of the nucleus will thus not reach the detector. Only decays near the nuclear surface will be registered which occur at low nuclear densities where mass shifts - assuming a density dependent mass modification - are also smaller. The sensitivity of the meson lineshape to in-medium modifications is thus reduced.

These caveats of the lineshape analysis have only been recognized in the course of the project. As an example, the results obtained with the Crystal Ball and TAPS detector system (Fig. 5) for  $\omega$  photoproduction off  $^{12}\text{C}$  and  $^{93}\text{Nb}$  targets will be discussed. High statistics have been accumulated in the energy range close to the production threshold [39], leading to an enhanced yield of low momentum  $\omega$  mesons.

Fig. 10 shows the  $\omega$  signal after subtraction of the background mostly arising from  $2\pi^0$  and  $\pi^0\eta$  events where one of the 4 decay photons was not registered in the Crystal Ball/TAPS detector system (for details of the background subtraction techniques, see [36]). The  $\omega$  signal in the Nb run is slightly broader than the reference signal obtained with the  $\text{LH}_2$  target [39]. In Fig. 10 the  $\omega$  signal on Nb is compared to GiBUU transport calculations [24, 35] for different in-medium scenarios. Although the statistics of the experiment has been considerably improved compared to previous studies [35, 36, 49] it is still not sufficient to distinguish different scenarios which differ only very little in the predicted line shape. This reflects the limited sensitivity of the lineshape analysis as discussed above. Only the scenario with a strong mass shift seems to be disfavored.

### 5.2.2 Excitation function of the $\omega$ and $\eta'$ mesons

As an alternative to the lineshape analysis, which showed a reduced sensitivity to in-medium modifications, infor-

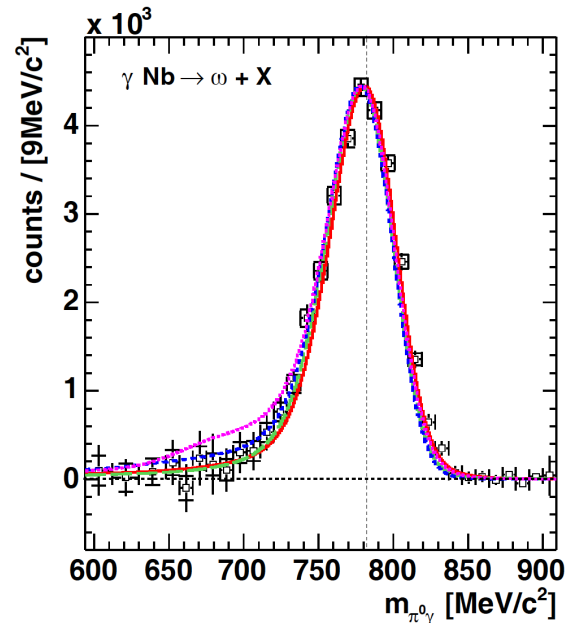


**Figure 10.** Comparison of the observed  $\pi^0\gamma$  invariant mass spectrum for the Nb target for inclusive analysis with GiBUU calculations [24] for different in-medium modification scenarios, assuming no in-medium modifications (red solid curve), only collisional broadening (green dashed curve), collisional broadening and mass shift by -14% at normal nuclear matter density (short dashed, blue curve) and mass shift without broadening (dotted, magenta curve) [39].

mation on the in-medium meson mass and the real part of the meson-nucleus potential can be extracted from the excitation function of the meson [24, 25]. In contrast to the lineshape analysis this method is sensitive to the nuclear density at the *production* point and hence it is applicable for all mesons, irrespective of their lifetime.

The experimental results for the  $\omega$  excitation function in comparison to theoretical calculations are shown in Fig. 11. Data were taken on a carbon target with the Crystal Ball and TAPS detector system at MAMI-C. The GiBUU transport model [21] has been applied to calculate the  $\omega$  excitation function for 6 different scenarios allowing for mass shifts up to  $-125$  MeV at normal nuclear density as it is shown in Fig. 11. It is again obvious that the data are not consistent with a strong mass shift scenario,  $V > 100$  MeV as predicted in [3, 13]. A  $\chi^2$ -fit of the data with the calculated excitation functions for the different scenarios gives a potential depth of  $V_{\omega A}(\rho = \rho_0) = -(42 \pm 17(\text{stat}) \pm 20(\text{syst}))$  MeV [50].

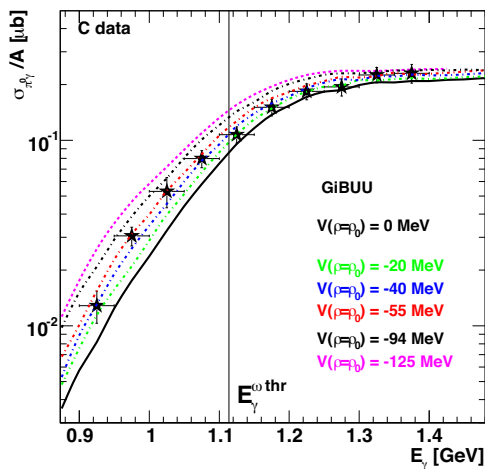


**Figure 11.** Measured excitation function for  $\omega$  meson in comparison to GiBUU transport calculations for several in-medium modification scenarios [50].

Experimental data for the  $\eta'$  excitation function in comparison to theoretical calculations are shown in Fig. 12 [37, 41]. In order to study the possible dependence of the real part of the  $\eta'$ -nucleus optical potential on the mass of the nucleus, the data were taken on  $^{12}\text{C}$  and  $^{93}\text{Nb}$  targets with the CBELSA/TAPS detector system. In both cases the data disfavor a deep real potential of  $V > 100$  MeV, as predicted in [11, 12]. While the  $\eta'$  cross section drops dramatically near the production threshold of  $E_\gamma = 1447$  MeV in case of the proton target [51], there is appreciable yield below this threshold in the reaction on the solid targets. There are several effects which can cause a non-zero cross section below 1447 MeV. This is on the one hand due to the Fermi motion of nucleons in the Nb target which gives rise to a distribution of the energy  $\sqrt{s}$  available in the centre-of-mass system for a given incident photon energy. On the other hand, also the mass of the meson might drop in a nuclear medium - as theoretically predicted - which lowers the production threshold and increases the phase space for meson production below the free threshold energy. The calculations have been performed within the first collision model based on the nucleon spectral function and described in detail in [25]. Starting from the measured differential

cross sections for  $\eta'$  production off the free proton and neutron [44, 51], the cross section for  $\eta'$  photoproduction off C and Nb is calculated in an eikonal approximation, taking the effect of the nuclear  $\eta'$  mean-field potential into account. The  $\eta'$  final-state absorption is determined by the inelastic in-medium  $\eta'N$  cross section taken to be  $\sigma_{inel} = 11$  mb, consistent with the result of transparency ratio measurements [22]. In the calculations for the Nb target  $\sigma_{inel} = 13$  mb has been assumed, consistent with the new results from [40]. The total nucleon spectral function is taken into account in the parametrization given in [52]. Thereby, the contribution of  $\eta'$  production from two-nucleon short-range correlations is taken into account. The calculations are improved in [37, 41] with respect to [25] as the momentum-dependent optical potential from [53], seen by the nucleons emerging from the nucleus in coincidence with the  $\eta'$  mesons, is accounted for as well.

The experimental data were compared with six different scenarios assuming depths of the  $\eta'$  real potential at normal nuclear matter density of  $V = 0, -25, -50, -75, -100$  and  $-150$  MeV, respectively (Fig. 12). The reduction in the incident photon flux due to photon shadowing has been taken into account by multiplying the observed  $\eta'$  yield by 1.17 [54–56]. The calculated cross sections for Carbon have been further scaled down - within the limits of the systematic uncertainties - by a factor of 0.83 to match the experimental excitation function data at incident photon energies above 2.2 GeV, where the difference between the various scenarios is very small. In the corresponding analysis of the Nb data [41] a rescaling of the theoretical calculations by 0.91 had to be applied. We are not aware of any missing physics in the calculations which might explain this systematic difference between data and calculations. In view of the systematic errors of the cross section data (23%) and the calculations (10-15%) a discrepancy cannot be claimed. The highest sensitivity to the  $\eta'$  potential depth is found for incident photon energies near and below the production threshold on the free nucleon. The excitation function data on both nuclei appear to be incompatible with  $\eta'$  mass shifts of  $-100$  MeV and more at normal nuclear matter density, as clearly seen in Fig. 12. A  $\chi^2$ -fit of the data with the calculated excitation functions for the different scenarios over the full range of incident energies gives a potential depth of  $-(40 \pm 6)$  MeV and  $-(40 \pm 12)$  MeV for C and Nb, respectively [37, 41].

It has been investigated whether the observed cross section enhancement relative to the  $V = 0$  MeV case could also be due to  $\eta'$  production on dynamically formed compact nucleonic configurations - in particular, on pairs of correlated nucleon clusters - which share energy and momentum. These effects have been studied experimentally [57] and theoretically [58, 59] in very near-threshold  $K^+$  production in proton-nucleus reactions. Applying the parametrization of the spectral function given by [52], in Fig. 12 (left: dot-dashed blue curve) has been shown that correlated high momentum nucleons contribute only about 10-15% to the  $\eta'$  yield in the incident energy

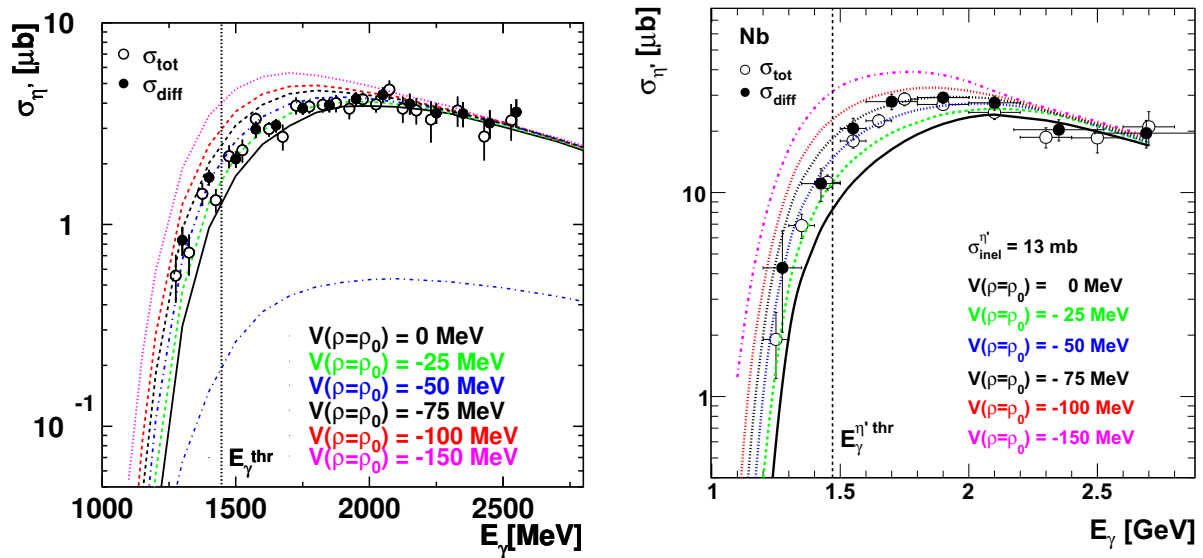


**Figure 12.** Measured excitation function for  $\eta'$  meson off  $^{12}\text{C}$  (left) and  $^{93}\text{Nb}$  (right), in comparison to theoretical calculations for different scenarios [37, 41]. The experimental data are extracted by integrating the differential cross sections (full circles) and by direct measurement of the  $\eta'$  yield in incident photon energy bins (open circles). The calculations are for  $\sigma_{\eta'N}=11$  mb (for C data) and for  $\sigma_{\eta'N}=13$  mb (for Nb data), and for potential depths:  $V=0$  MeV (black line),  $-25$  MeV (green),  $-50$  MeV (blue),  $-75$  MeV (black dashed),  $-100$  MeV (red) and  $-150$  MeV (magenta) at normal nuclear density, respectively, and using the full nucleon spectral function. The dot-dashed blue curve (in the left spectrum) is calculated for correlated intranuclear nucleons only.

regime above 1250 MeV [37]. The observed cross section enhancement can therefore be attributed mainly to the lowering of the  $\eta'$  mass in the nuclear medium.

### 5.2.3 Momentum distribution of the $\omega$ and $\eta'$ mesons

As discussed in section 2, the momentum distribution of the mesons is also sensitive to the potential depth and has been investigated as well. Fig. 13 shows the momentum distribution of  $\omega$  mesons in comparison to GiBUU simulations for different in-medium modification scenarios. The  $\omega$  momentum distributions measured for near-threshold photo production off  $^{12}\text{C}$  and  $^{93}\text{Nb}$  do not support calculations predicting mass shifts as large as  $-16\%$  [3, 13].

The measured momentum differential cross sections for  $\eta'$  meson photoproduction off C [37] and Nb [41] are shown in Fig. 14. The average momentum in both cases is  $\approx 1.1$  GeV/c. Bin sizes of  $0.1$  GeV/c for C data and  $\geq 0.2$  GeV/c for Nb data have been chosen which are large compared to the momentum resolution of  $25\text{-}50$  MeV/c deduced from the experimental energy resolution and from Monte Carlo simulations. The  $\eta'$  momentum distributions have been calculated for the incident photon energy range  $1.3\text{-}2.6$  GeV and for different potential depths  $V = 0, -25, -50, -75, -100$  and  $-150$  MeV. The comparison of these calculations with the data again exclude strong  $\eta'$  mass shifts. A  $\chi^2$ -fit of the data with the calculated momentum distributions for the different scenarios over the full range of incident energies gives a potential depth of  $-(32\pm 11)$  MeV and  $-(45\pm 20)$  MeV off C and Nb, respectively [41].

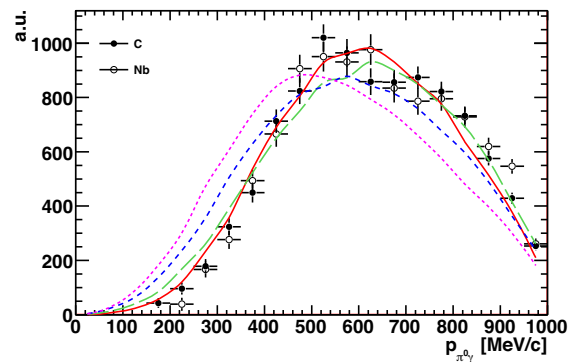


**Figure 13.** Acceptance corrected  $\omega$  momentum distribution for incident photon energies of 900 to 1300 MeV and for  $^{12}\text{C}$  and  $^{93}\text{Nb}$  targets, compared to the theoretical predictions for different in-medium modifications scenarios: no modification (solid red line), collisional broadening (dashed green line), collisional broadening plus mass shift (dashed blue line) and mass shift (magenta line). All distributions are normalized to the same area [39].

### 5.2.4 The $\omega$ -nucleus real potential at low momenta

As has been pointed in 5.2.3, the average momentum of  $\omega$  and  $\eta'$  mesons was around  $0.6 - 1$  GeV/c (see Fig. 13, Fig. 14). To study the possible momentum dependence of the real part of the meson-nucleus optical potential an experiment has been performed to produce  $\omega$  mesons with low momenta ( $< 500$  MeV/c). In the reaction  $\gamma\text{C} \rightarrow \omega\text{p} \rightarrow \pi^0\gamma\text{p}$  the proton has been measured in the TAPS

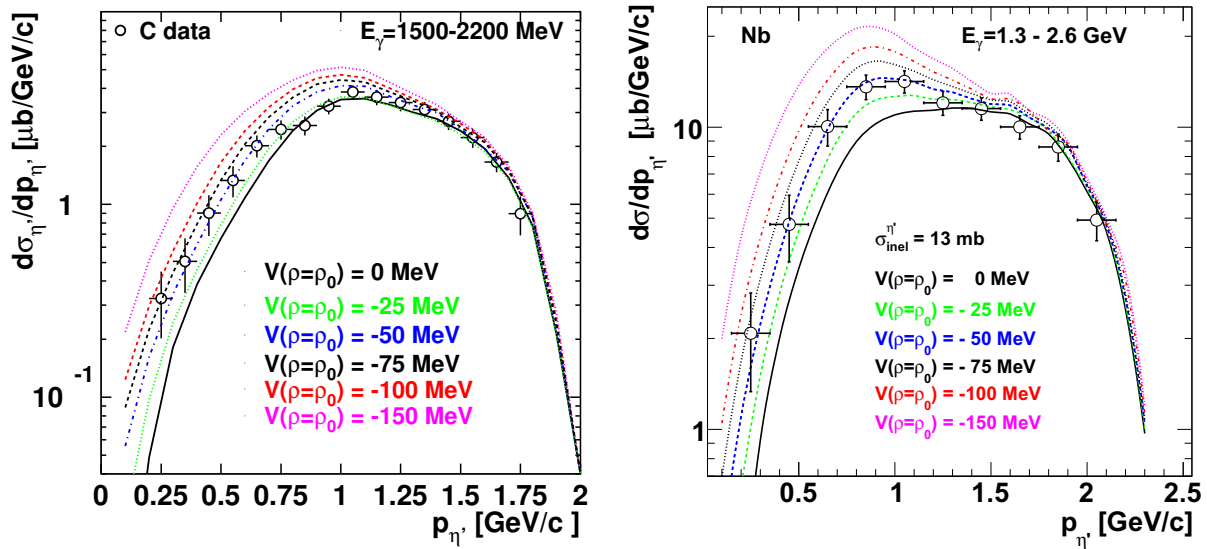


**Figure 14.** Left: Momentum distribution for  $\eta'$  photoproduction off C for the incident photon energy range 1500-2200 MeV. The calculations are for  $\sigma_{\eta'N}=11$  mb and have been reduced by a factor 0.75 (see text) [37]. Right: Momentum distribution for  $\eta'$  photoproduction off Nb for the incident photon energy range 1.3-2.6 GeV. The calculations are for  $\sigma_{\text{inel}}^{\eta'}=13$  mb and have been multiplied by a factor 0.83 (see text) [41]. In both spectra the theoretical curves are for potential depths  $V = 0, -25, -50, -75, -100$  and  $-150$  MeV at normal nuclear density. The color code is identical to the one in Fig. 12.

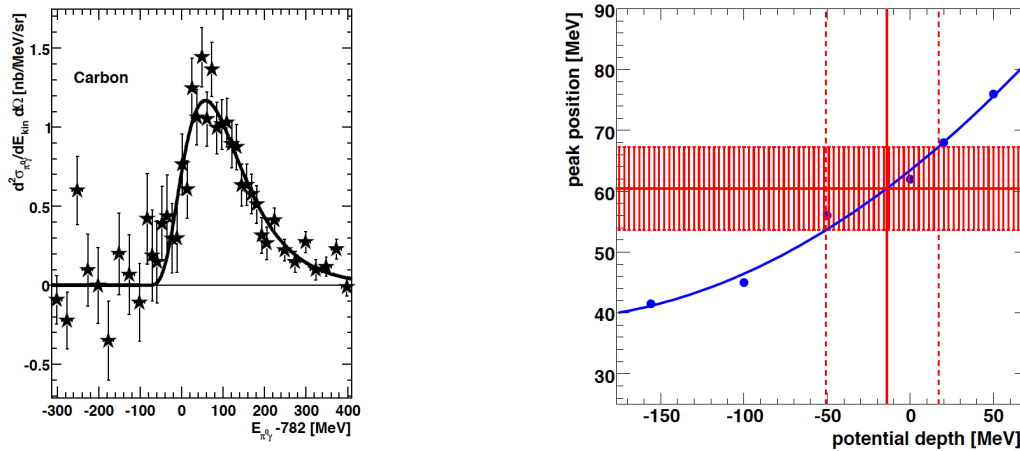


**Figure 15.** Left: Differential cross section for the photo production of  $\omega$ -mesons off C in coincidence with protons in  $\Theta_p = 1^\circ - 11^\circ$  as a function of the total energy of the  $\pi^0\gamma$  pairs minus 782 MeV. The data have been fitted with the Novosibirsk function [62]. Right: Correlation between the potential depth and the peak position in the total energy distribution. The (blue) points represent the peak positions in the total energy distribution for the different scenarios [11, 63–65]. The (blue) solid curve is a fit to the points. The red dashed area corresponds to the peak position of  $(60.5 \pm 7)$  MeV [61].

detector (see Fig. 4 right) covering the polar angle range  $\Theta_p = 1^\circ - 11^\circ$ . In this case the forward going proton takes over most of the momentum of the incoming photon beam. Being so low in energy, the  $\omega$ -mesons are particularly sensitive to the  $\omega$  nucleus potential. In case of a strong repulsive (attractive) interaction one would expect the peak in the kinetic energy distribution to be shifted to higher (lower) energies for the C target. The sensitivity of the peak position in the kinetic energy distribution on the potential depth, studied in [61], can be exploited to deduce the depth of the real part of the  $\omega$ -nucleus potential.

The experimental data for the  $\omega$  kinetic energy distribution are shown in Fig. 15 (left). The data have been fitted with the Novosibirsk function [62], giving a peak position of  $(60.5 \pm 7)$  MeV [61]. The correlation between the potential depth and the peak in the kinetic energy distribution is plotted in Fig. 15 (right). A comparison with the experimentally determined peak position indicates a potential depth of  $-(15 \pm 35)$  MeV which appears to be too small to allow for the formation and population of  $\omega$  mesic states, in particular in view of the large in-medium width of  $\approx 90$  MeV (see 5.3).



**Figure 16.** Depths of the real part of the  $\omega$  (left) and  $\eta'$  (right) -nucleus potential determined by analyzing the excitation function and the momentum distributions for C [37, 50] (full black circles) and for Nb [41] (red triangles). The weighted overall average is indicated by a blue square and the shaded area. The vertical hatched lines mark the range of systematic uncertainties

### 5.2.5 Conclusions on the real part of the $\omega$ - and $\eta'$ -nucleus optical potential

Combining the results from the analysis of the excitation function and the peak position from the kinetic energy distribution an average depth of the real part of the  $\omega$ -C optical potential of  $V(\rho = \rho_0) = -(29 \pm 19(\text{stat}) \pm 20(\text{syst}))$  MeV is obtained Fig. 16 (left).

From the analysis of the excitation functions and the momentum distributions and by proper weighting of the errors a depth of the real part of the  $\eta'$ -C and -Nb optical potential of  $V(\rho = \rho_0) = -(39 \pm 7(\text{stat}) \pm 15(\text{syst}))$  MeV is obtained (see Fig. 16 (right)). The systematic error quoted is mainly due to uncertainties in normalizing the calculations to the data. The sensitivity of the result on this normalization has been studied by varying the normalization factor between 0.7 to 1.0 - well within the systematic errors of the cross section determinations.

This result for  $V(\rho = \rho_0)$  is consistent with predictions of the  $\eta'$ -nucleus potential depth within the Quark-Meson Coupling model (QMC) [16] and with calculations in [60] but does not support larger mass shifts as discussed in [11, 14].

### 5.3 The imaginary part of the meson-nucleus optical potential

Figure 17 presents the differential cross sections per nucleon for  $\omega$  and  $\eta'$  photoproduction off carbon and niobium as a function of the meson momentum for incident photon energies of 1.2-2.9 GeV [40]. The cross sections include a 15% correction for absorption of the incoming photon beam (photon shadowing) for both nuclear targets [54–56]. The distributions show a maximum at around 800 MeV/c and 1000 MeV/c for the  $\omega$  and  $\eta'$ , respectively, and fall off towards higher momenta. The average momenta, given in Fig. 17, are close to 1000 MeV/c. To determine the meson attenuation in nuclei and the inelastic meson-nucleon cross sections as a function of the meson momentum, the transparency ratio [26] is deduced from the data as defined in Eq.5. To suppress nuclear effects not related to meson absorption, the transparency ratio is not taken relative to the free nucleon but rather to a nucleon in a light nucleus like carbon as suggested in [47].

The momentum dependence of the transparency ratio for a meson  $m$  is thus obtained by dividing the differential inclusive meson production cross sections (see Fig. 17) for niobium by the one for carbon according to

$$T_{\text{Nb/C}}^m = \frac{12 \cdot \sigma_{\gamma\text{Nb} \rightarrow mX}}{93 \cdot \sigma_{\gamma\text{C} \rightarrow mX}}, \quad (6)$$

where 12 and 93 are the nuclear mass numbers of carbon and niobium, respectively. The resulting transparency ratios as a function of the meson momentum are shown in Fig. 18. Consistent with earlier measurements [37, 48], a slight increase with momentum is observed for the  $\omega$  meson while for the  $\eta'$  meson the transparency ratio is almost independent of momentum. Differences between the transparency ratios in the present measurements and the earlier ones reflect the systematic uncertainties of the measurements. For the present data the thick error bars (red) in Fig. 18 and subsequent figures represent the statistical errors while the thinner error bars (black) include the systematic errors added in quadrature.

The interpretation of the transparency ratio in terms of meson absorption will only give reliable results if two-step production processes are negligible, where e.g. a pion is produced in an initial step followed by production of the meson of interest in a subsequent pion-induced reaction on another nucleon within the nucleus. As shown in [22], two-step processes are negligible for  $\omega$  and  $\eta'$  mesons since the spectral distribution of pions falls off towards higher energies and - at the required pion momenta of  $\approx 1.3$  and  $1.5$  GeV/c - pion induced meson production cross sections are only  $\approx 2.5$  mb and  $0.1$  mb, respectively, compared to the total reaction cross section of about 30-40 mb [23]. Consequently, two-step processes are neglected in the subsequent analysis of the transparency ratio.

Following [22, 25, 48] the in-medium meson width is deduced from the measured transparency ratio within a Glauber model in the high energy eikonal approximation (for details see [40]). Hereby, the in-medium width  $\Gamma(\rho)$  is assumed to depend linearly on the nuclear density  $\rho$ :

$$\Gamma(\rho) = \Gamma_0 \cdot \frac{\rho}{\rho_0}, \quad (7)$$

where  $\Gamma_0$  is the momentum dependent width at normal nuclear matter density. As a result, the in-medium width  $\Gamma_0$

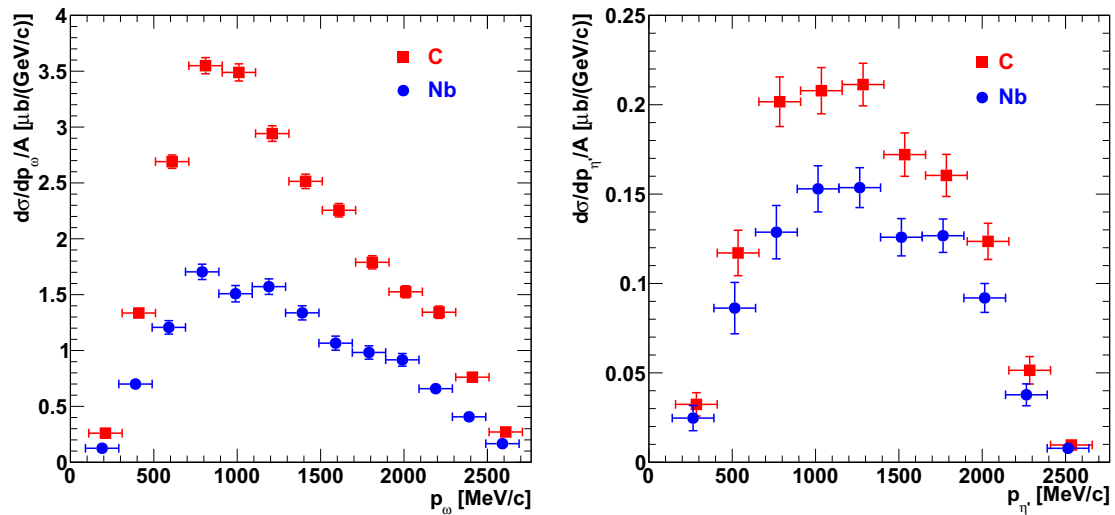


**Figure 17.** Differential cross section per nucleon for (Left)  $\omega$  and (Right)  $\eta'$  photoproduction off carbon (red squares) and niobium (blue circles) for the incident photon energies of 1.2-2.9 GeV. The data points for carbon are shifted by +10 MeV/c and for niobium by -10 MeV/c to avoid an overlap of the error bars.

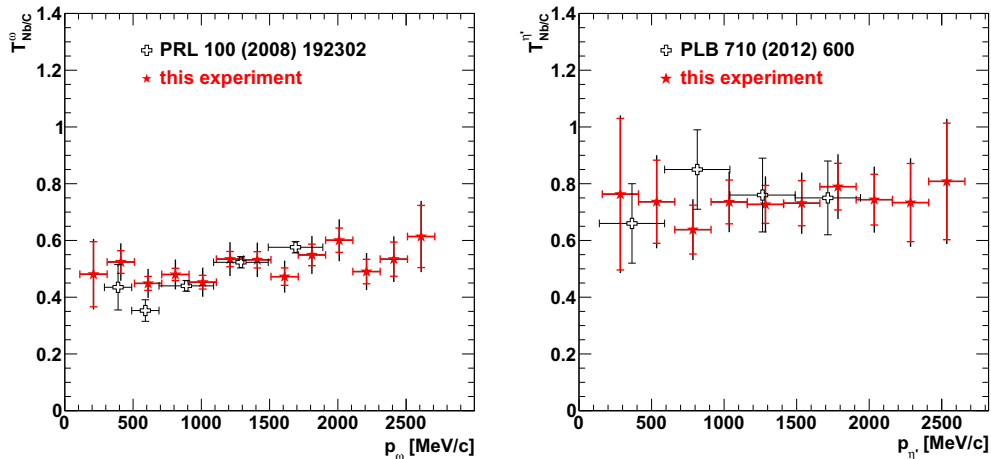


**Figure 18.** The transparency ratio according to Eq. 6 for (Left)  $\omega$  and (Right)  $\eta'$  photoproduction off carbon and niobium (red stars) in comparison to earlier measurements (open crosses) [22, 48]. The data points of the present work are shifted by +10 MeV/c and the previously published data by -10 MeV/c to avoid an overlap of the error bars. For the present data the thick error bars (red) represent the statistical errors. The thin error bars (black) include the systematic errors added in quadrature.

is shown in Fig. 19 as a function of the  $\omega$  and  $\eta'$  momentum, respectively. The non-linearity in the correlation between transparency ratio and in-medium width introduces strongly asymmetric error bars. Within errors, the results are consistent with previous measurements [22, 48, 66]. It is immediately apparent that the  $\omega$  widths are larger than the  $\eta'$  widths by about a factor three. The finer binning in the present data also reveals more clearly a variation of the widths with momentum, indicating a rise with momentum at small momenta and a fall-off towards higher momenta.

The data for the  $\omega$  meson are compared to calculations of the in-medium  $\omega$  width. Cabrera and Rapp [20] and

Ramos *et al.* [19] have studied the width of the  $\omega$  meson in cold nuclear matter as a function of the nuclear density and the meson 3-momentum. Both groups independently find that the main contribution to the in-medium  $\omega$  width is determined by the  $\omega \rightarrow \rho\pi$  channel whereby the dressing of the  $\pi$  and  $\rho$  propagator in the medium is essential. Thus, they argue that the  $\pi\rho$  cloud is the main agent for the in-medium broadening of the  $\omega$  meson. Both groups obtain in-medium  $\omega$  widths of the order of 100-200 MeV, somewhat larger than observed experimentally. They differ in the partitioning into the  $\pi$  and  $\rho$  modifications and obtain differences in the 3-momentum dependence of the

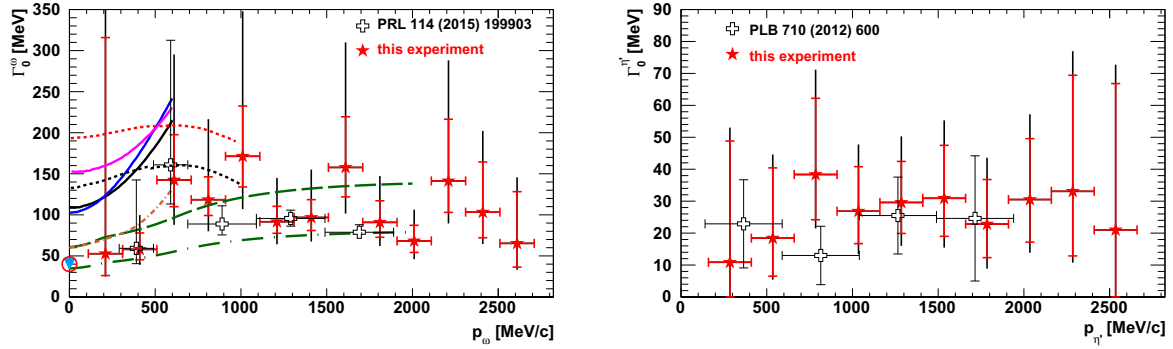


**Figure 19.** In-medium width  $\Gamma_0$  of (Left)  $\omega$  and (Right)  $\eta'$  mesons as a function of the meson momentum (red stars), derived from the data presented in Fig. 18, in comparison to earlier measurements (open crosses) [22, 48, 66]. The data points of the present work are shifted by +10 MeV/c and the previously published data by -10 MeV/c to avoid an overlap of the error bars (symbols as in Fig. 18). The solid curves correspond to calculations by Ramos *et al.* [19], the short dashed curves to calculations by Cabrera and Rapp [20] for different model assumptions (see text). The brown dashed-dotted curve shows the momentum dependence of the  $\omega$  in-medium width calculated in a coupled-channel resonance model [18]. The long dashed green curves correspond to different options for the in-medium  $\omega$  width used in GiBUU simulations [21]. The blue triangle and the red open circle represent the widths calculated for an  $\omega$  meson at rest in the nuclear medium in [13, 17], respectively.

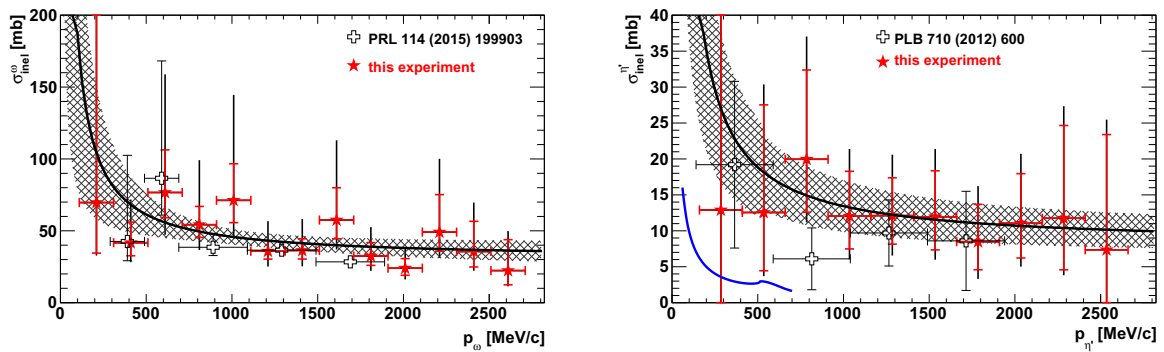


**Figure 20.** Left:  $\omega$  inelastic cross section and Right:  $\eta'$  cross section as a function of the momentum (red stars) [40] in comparison to earlier measurements (open crosses) [22, 48, 66].

$\omega$  width. While Cabrera and Rapp [20] find a moderate momentum dependence, Ramos *et al.* [19] get an almost linear increase of the width with momentum. Alternatively, Klingl *et al.* [13], Lutz *et al.* [17] and Mühlich *et al.* [18] consider the coupling of the  $\omega$  meson to nucleon resonances as the main effect driving the in-medium broadening of the  $\omega$  meson. In fact, the data are closer to the momentum dependence of the  $\omega$  in-medium width calculated in a coupled-channel resonance model [18] and are only slightly larger at low momenta than the width of 40 MeV calculated for the  $\omega$  at rest in the nuclear medium [13, 17]. The statistics of the present experiment is unfortunately not sufficient to clearly discriminate between these different theoretical approaches.

From the in-medium widths  $\Gamma_0$  of Fig. 19 inelastic cross sections  $\sigma_{\text{inel}}$  can be derived, using the low-density approximation which relates the in-medium meson width  $\Gamma(\rho = \rho_0) = \Gamma_0$  at normal nuclear matter density  $\rho_0$  to the inelastic meson-nucleon cross section  $\sigma_{\text{inel}}$  by

$$\Gamma(\rho = \rho_0) = \Gamma_0 = \hbar c \cdot \rho_0 \cdot \sigma_{\text{inel}} \cdot \beta. \quad (8)$$

Here,  $\beta$  is the relative velocity of the meson in the nuclear restframe. The resulting inelastic cross sections are shown in Fig. 20 as a function of the meson momentum. To compare the data to a parametrization frequently used in the literature, the data for both mesons have been fitted with an ansatz

$$\sigma_{\text{inel}}[\text{mb}] = a + \frac{b}{p[\text{GeV}/c]}, \quad (9)$$

as proposed by Lykasov *et al.* [67] and used as parametrization in GiBUU transport simulations [21]. The present inelastic  $\eta'$  cross section data (Fig. 20 (right)) shows a mean value of  $(13 \pm 3)$  mb, slightly larger but consistent with the earlier result of  $(10.3 \pm 1.4)$  mb reported in [22]. The experimental data are compared to calculations by Oset and Ramos [68]. They have studied the  $\eta'$ -nucleon interaction within a chiral unitary approach, including  $\pi N$  and  $\eta N$  coupled channels, which yields a very weak  $\eta' N$  interaction. The  $\eta' N$  amplitude is substantially enhanced when vector meson-baryon states are included in the coupled channel scheme via normal and anomalous couplings

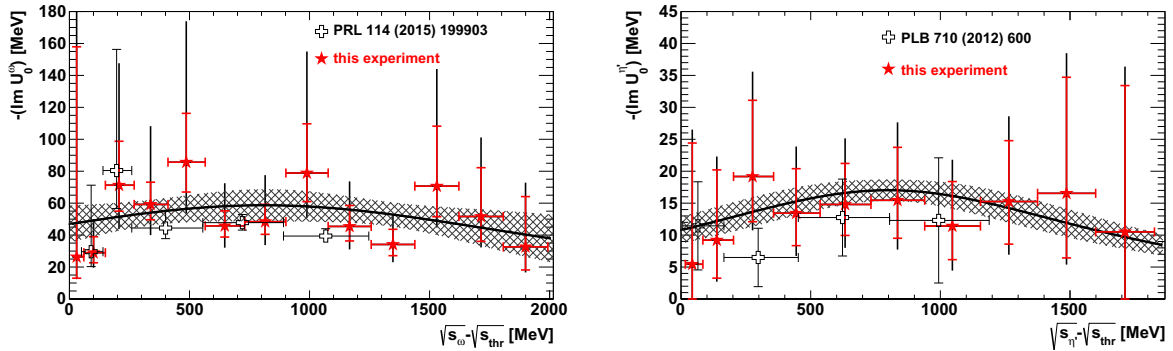


**Figure 21.** Imaginary part of the (Left)  $\omega$ -nucleus and (Right)  $\eta'$ -nucleus optical potential as a function of the available energy in the meson- $^{93}\text{Nb}$  system (red stars) [40] in comparison to earlier measurements (open crosses) [22, 48, 66]. The solid curves are Breit-Wigner fits to the present data. The shaded areas indicate a confidence level of  $\pm 1\sigma$  of the fit curve taking statistical and systematic errors into account.

of pseudo-scalar to vector mesons. In this approach inelastic  $\eta'N$  cross sections rising from about 3 mb at  $p_{\eta'} = 600$  MeV/c to about 20 mb at  $p_{\eta'} = 50$  MeV/c are predicted. The calculations seem to underestimate the experimentally determined inelastic  $\eta'$  cross section. This may not be surprising since multi-particle production, probably dominant because of the large  $\eta'$  mass, has not been considered in [68].

As a final step, the momentum dependence of the in-medium  $\omega$  and  $\eta'$  widths from Fig. 19 can be converted into the dependence of the imaginary part of the  $\omega$ - and  $\eta'$ -nucleus potential as a function of the available energy in the meson- $^{93}\text{Nb}$  system, as shown in Fig. 21. The imaginary part of the potential  $\text{Im}U$  at normal nuclear matter density is just half of the in-medium width  $\Gamma_0$  (see Fig. 19). The finer binning of the present data allows a more reliable extrapolation towards the production threshold by fitting the data. Several fit functions have been applied (polynomial of 1st. and 2nd. order, Gaussian, Breit-Wigner). The range of  $-\text{Im}U(0)$  values obtained for different fit functions reflects the systematic uncertainties. For the  $\omega$  meson the modulus of the imaginary part of the meson nucleus potential near threshold is found to be  $(48 \pm 12(\text{stat}) \pm 9(\text{syst}))$  MeV comparable to the modulus of the real part of about 30 MeV, determined in [50, 61, 69]. For the  $\eta'$  meson the extrapolation towards the production threshold yields an imaginary potential of  $(13 \pm 3(\text{stat}) \pm 3(\text{syst}))$  MeV, corresponding to an imaginary part of the  $\eta'$  scattering length  $\text{Im}(a_{\eta'N}) = (0.16 \pm 0.05)$  fm. This is about a factor two smaller than obtained in the direct determination of the  $\eta'N$  scattering length from an analysis of near threshold  $\eta'$  production in the  $pp \rightarrow pp\eta'$  reaction [70]. The error bars of both completely independent determinations do, however, almost overlap.

## 6 Meson-nucleus bound states

The existence of deeply bound pionic states is clearly established [71–74]. These systems are bound by the attractive Coulomb interaction between a negatively charged

pion and the positively charged nucleus. The superposition with the strong interaction, which is repulsive at low pion momenta, leads to a potential pocket near the nuclear surface and consequently to a halo-like  $\pi^-$  distribution around the nucleus [75]. Thus pions are only weakly absorbed, giving rise to rather narrow bound states which facilitated their experimental observation.

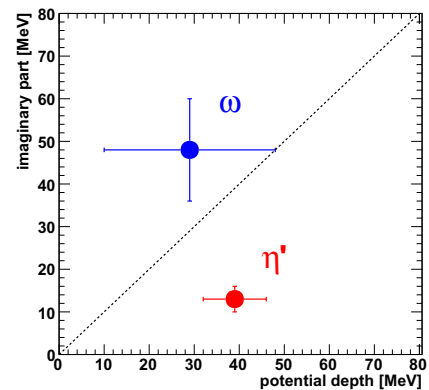


**Figure 22.** The imaginary part versus the real part of the meson-nucleus potential for  $\omega$  and  $\eta'$  mesons

As outlined in the previous sections, the interaction of neutral mesons with nuclei has been studied to find out whether meson-nucleus states might exist as well, only bound by the strong interaction. Here, the meson-nucleus interaction has to be sufficiently attractive and the meson absorption in nuclei should be relatively weak to allow the formation of relatively narrow states. Considering the results obtained for the  $\omega$  and  $\eta'$ -nucleus potentials it is evident that the  $\eta'$  meson is a much better candidate for the formation of meson-nucleus bound states than the  $\omega$  meson since we found for the  $\eta'$  meson that  $|W| \ll |V|$ , while the opposite was observed for the  $\omega$  meson, as illustrated in Fig. 22. For the  $\eta'$  meson there is a possibility for the existence of relatively narrow bound states while for the  $\omega$  meson the imaginary potential is comparable to the

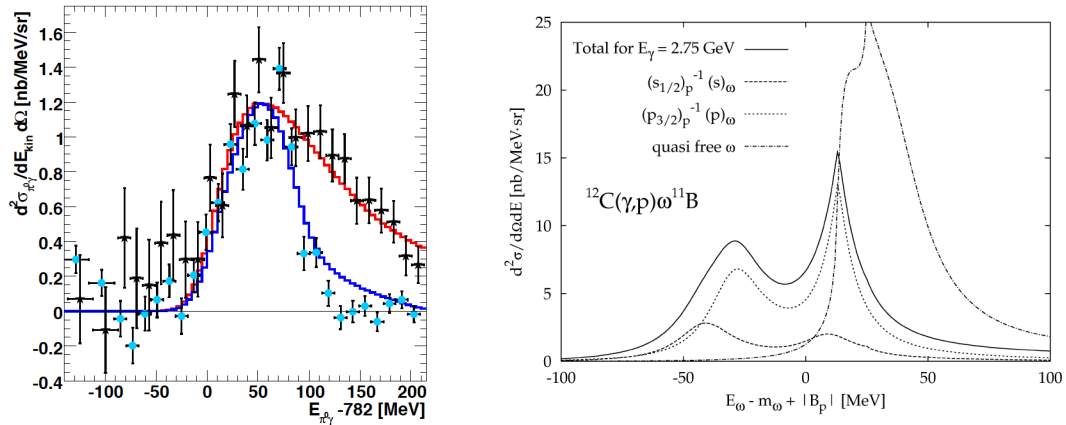


**Figure 23.** Left: Kinetic energy distribution of the  $\omega$  meson off Carbon (black stars) compared with the kinetic energy distribution of the  $\omega$  meson off the free proton (full blue circles). The LH<sub>2</sub> data are normalized to the C data in the peak of the total energy distribution. The experimental distributions are compared to Monte Carlo simulations (LH<sub>2</sub> : blue histogram; C: red histogram), taking the Fermi motion of nucleons into account for the C target. All distributions request the detection of a proton in the polar angular range  $1^\circ - 11^\circ$  and are normalized to the fitted peak height for C. The Monte Carlo simulations are folded with the experimental resolution of  $\sigma_E \approx 16$  MeV [61]. Right: Missing energy spectra calculated by Marco and Weise [76] for the  $^{12}\text{C}(\gamma, p)\omega^{11}\text{B}$  reaction at  $E_\gamma = 2.75$  GeV. Dotted lines represent the contributions from two particular combinations of bound  $\omega$  and proton-hole states.

real one and only broad structures can be expected which makes it difficult to detect them experimentally.

Nevertheless, an attempt to search for  $\omega$  mesic states has been performed [61]. Using the  $\gamma^{12}\text{C} \rightarrow \pi^0\gamma + p + X$  reaction with the proton detected at forward angles in TAPS, the distribution of the total energy  $E_\omega$  of  $\pi^0\gamma$  pairs with an invariant mass in the  $\omega$  mass range has been measured and compared to the reaction  $\gamma p \rightarrow \pi^0\gamma p$  on a liquid hydrogen target as shown in Fig. 23 (Left) [61]. Positive values  $E_\omega - m_\omega$  give the kinetic energy of the  $\omega$  in quasi-free production, while events with negative values may signal the decay of  $\omega$ - $^{11}\text{B}$  bound states via  $\pi^0\gamma$  emission. Comparing the energy distributions measured for both targets, some tailing is observed for the carbon target in the fall off towards lower energies which is not observed for the reaction on the free proton, even if one accounts for the smearing due to Fermi motion which is taken into account in the Monte Carlo simulation. The  $\pi^0\gamma$  cross section in the energy range from -100 to 0 MeV is on average  $(0.3 \pm 0.1)$  nb MeV $^{-1}$ sr $^{-1}$ . Correcting for the effective branching ratio for in-medium  $\omega \rightarrow \pi^0\gamma$  decays of  $\approx 1.5\%$  [61] a population cross section of  $(22 \pm 7)$  nb MeV $^{-1}$ sr $^{-1}$  is deduced which is of the order of magnitude for the formation of  $\omega$  mesic states as calculated by Marco and Weise [76] (see Fig. 23 (Right)). Structures at negative energies which would indicate the population and decay of bound  $\omega$ - $^{11}\text{B}$  states are, however, not observed. The yield at negative energies may arise from the strong in-medium broadening of the  $\omega$  meson, discussed in section 5.3.

Since the  $\eta'$  meson is the better candidate for the search of mesic states several corresponding experiments have been launched. At the Fragment Separator (FRS) at GSI an experiment to search for  $\eta'$  bound states has been performed via missing mass spectroscopy in the  $^{12}\text{C}(p, d)$  reaction in almost recoil free kinematics [77] and is being analysed. An alternative approach is the photopro-

duction of  $\eta'$  mesons in the  $^{12}\text{C}(\gamma, p)$  reaction, again in almost recoil-free kinematics. In the ongoing experiment at the LEPS2 facility (Spring8) [78] the missing mass spectroscopy is combined with detecting the decay of the  $\eta'$  mesic state in a semi-exclusive measurement. An analogous photoproduction measurement has been proposed for the BGO-OD setup at the ELSA accelerator in Bonn [79]. A semi-exclusive measurement has also been considered for the Super-FRS at FAIR [65].

## 7 Conclusion

The photoproduction of  $\omega$  and  $\eta'$  mesons off nuclei has been studied in the 1-3 GeV energy range to extract information on the in-medium properties of these mesons. The interaction of mesons with nuclei and the in-medium effects have been described with an optical model, comprising a real part, associated with the mass modification in the nuclear medium, and an imaginary part, accounting for the absorption of mesons in nuclei. For the  $\omega$ - and  $\eta'$ - nucleus optical potential values of  $U_{\omega A}(\rho = \rho_0) = -(29 \pm 19(\text{stat}) \pm 20(\text{syst})) + i(48 \pm 12(\text{stat}) \pm 9(\text{syst}))$  MeV and  $U_{\eta' A}(\rho = \rho_0) = -(39 \pm 7(\text{stat}) \pm 15(\text{syst})) + i(13 \pm 3(\text{stat}) \pm 3(\text{syst}))$  MeV have been obtained. The latter measurement establishes for the first time an in-medium mass drop of a pseudoscalar meson at normal nuclear matter density. Although not very deep, the real part of the  $\eta'$ - nucleus potential is about three times larger than the imaginary part and may thus allow the existence and observation of  $\eta'$ -nucleus states, only bound by the strong interaction. Corresponding experiments are ongoing.

The results reported here have been obtained within the CBELSA/TAPS collaboration and would not have been achieved without the work of strongly engaged and highly motivated PhD-

students and postdocs, in particular F. Dietz, S. Friedrich, M. Kotulla, K. Makonyi, M. Thiel, and D. Trnka. M. Kotulla acted as co-projectleader in July 2008 before leaving our group. The support by the staff members of the ELSA accelerator and collaborating universities is highly appreciated. This project benefitted a lot from the close collaboration with project B5 (U. Mosel, P. Mühlich and J. Weil) regarding the interpretation of model calculations and the link between theoretical predictions and experimental observables, provided by transport calculations. The work reported here would not have been possible without the support from the Deutsche Forschungsgemeinschaft within the SFB/TR16.

## References

- [1] V.- Bernard and Ulf-G. Meißner, Nucl. Phys. A **489**, 647 (1988).
- [2] G. E. Brown and M. Rho, Phys. Rev. Lett. **66**, 2720 (1991).
- [3] T. Hatsuda and S. Lee, Phys. Rev. C **46**, R34 (1992).
- [4] R. Rapp, J. Wambach, H. van Hees, in: R. Stock (Ed.), *Relativistic Heavy-Ion Physics*, in: Landolt Börnstein (Springer), New Series, vol. I/23A, 4-1 (2010)
- [5] R. Hayano and T. Hatsuda, Rev. Mod. Phys. **82**, 2949 (2010)
- [6] S. Leupold, V. Metag, and U. Mosel, Int. J. Mod. Phys. E **19**, 147 (2010)
- [7] S. Klimt et al., Nucl. Phys. A **516**, 429 (1990).
- [8] V. Bernard, R. L. Jaffe and U.-G. Meißner, Nucl. Phys. B **308**, 753 (1988).
- [9] S. Leupold, W. Peters, and U. Mosel, Nucl. Phys. A **628**, 311 (1998).
- [10] V. Bernard and Ulf-G. Meißner, Phys. Rev. D **38**, 1551 (1988).
- [11] H. Nagahiro, M. Takizawa, and S. Hirenzaki, Phys. Rev. C **74**, 045203 (2006).
- [12] H. Nagahiro and S. Hirenzaki, Phys. Rev. Lett. **94**, 232503 (2005).
- [13] F. Klingl et al., Nucl. Phys. A **610**, 297 (1997), Nucl. Phys. A **650**, 299 (1999).
- [14] S. Sakai and D. Jido, Phys. Rev. C **88**, 064906 (2013).
- [15] K. Saito, K. Tsushima, and A. W. Thomas, Prog. Part. Nucl. Phys. **58**, 1 (2007).
- [16] S. D. Bass and A. W. Thomas, Phys. Lett. B **634**, 368 (2006).
- [17] M. Lutz et al., Nucl. Phys. A **706**, 431 (2002).
- [18] P. Mühlich et al., Nucl. Phys. A **780**, 187 (2006).
- [19] A. Ramos, L. Tolos, R. Molina, and E. Oset, Eur. Phys. J. A **49**, 148 (2013).
- [20] D. Cabrera and R. Rapp, Phys. Lett. B **729**, 67 (2014).
- [21] O. Buss et al., Phys. Rep. **512**, 1 (2012).
- [22] M. Nanova et al., CBELSA/TAPS Collaboration, Phys. Lett. B **710**, 600 (2012).
- [23] K. A. Olive et al., Particle Data Group, Chin. Phys. C **38**, 090001 (2014).
- [24] J. Weil, U. Mosel, and V. Metag, Phys. Lett. B **723**, 120 (2013).
- [25] E. Ya. Paryev, J. Phys. G: Nucl. Part. Phys. **40**, 025201 (2013).
- [26] D. Cabrera et al., Nucl. Phys. A **733**, 130 (2004).
- [27] D. Husmann and W. J. Schwillie, Phys. Bl. **44**, 40 (1988).
- [28] W. Hillert, Eur. Phys. J. A **28**, 139 (2006).
- [29] D. Elsner et al., CBELSA/TAPS Collaboration, Eur. Phys. J. A **33**, 147 (2007).
- [30] E. Aker et al., Nucl. Instr. and Meth. A **321**, 69 (1992).
- [31] G. Suft et al., Nucl. Instr. and Meth. A **538**, 416 (2005).
- [32] R. Novotny et al., IEEE Trans. Nucl. Sci. **38**, 392 (1991).
- [33] A. R. Gabler et al., Nucl. Instr. and Meth. A **346**, 168 (1994).
- [34] T. Mertens et al., CBELSA/TAPS Collaboration, Eur. Phys. J. A **38**, 195 (2008).
- [35] M. Nanova et al., CBELSA/TAPS Collaboration, Eur. Phys. J. A **47**, 16 (2011).
- [36] M. Nanova et al., CBELSA/TAPS Collaboration, Phys. Rev. C **82**, 035209 (2010).
- [37] M. Nanova et al., CBELSA/TAPS Collaboration, Phys. Lett. B **727**, 417 (2013).
- [38] A. Thiel et al., CBELSA/TAPS Collaboration, Phys. Rev. Lett. **109**, 102001 (2012).
- [39] M. Thiel et al., Eur. Phys. J. A **49**, 132 (2013).
- [40] S. Friedrich et al., CBELSA/TAPS Collaboration, Eur. Phys. J. A **52**, 297 (2016).
- [41] M. Nanova et al., CBELSA/TAPS Collaboration, Phys. Rev. C **94**, 025205 (2016).
- [42] R. Brun et al., GEANT, CERN/DD/ee/84-1 (1986).
- [43] F. Dietz et al., CBELSA/TAPS Collaboration, Eur. Phys. J. A **51**, 6 (2015).
- [44] I. Jaegle et al., CBELSA/TAPS Collaboration, Eur. Phys. J. A **47**, 11 (2011).
- [45] C. Cioffi degli Atti and S. Simula, Phys. Rev. C **53**, 1689 (1996).
- [46] J. G. Messchendorpl et al., Eur. Phys. J. A **11**, 95 (2001).
- [47] M. Kaskulov et al., Phys. Rev. C **75**, 064616 (2007).
- [48] M. Kotulla et al., CBELSA/TAPS Collaboration, Phys. Rev. Lett. **100**, 192302 (2008).
- [49] D. Trnka et al., CBELSA/TAPS Collaboration, Phys. Rev. Lett. **94**, 192203 (2005).
- [50] V. Metag et al., A2 Collaboration, Prog. Part. Nucl. Phys. **67**, 530 (2012).
- [51] V. Crede et al., CBELSA/TAPS Collaboration, Phys. Rev. C **80**, 055202 (2009).
- [52] S. V. Efremov and E. Ya. Paryev, Eur. Phys. J. A **1**, 99 (1998).
- [53] Z. Rudy et al., Eur. Phys. J. A **15**, 303 (2002).
- [54] T. Falter, S. Leupold, and U. Mosel, Phys. Rev. C **64**, 024608 (2001).
- [55] N. Bianchi et al., Phys. Rev. C **54**, 1688 (1996).

- [56] V. Muccifora *et al.*, Phys. Rev. C **60**, 064616 (1999).  
[57] M. Debowski *et al.*, Acta Phys. Polonica B **27**, 3015 (1996).  
[58] A. Sibirtsev, W. Cassing, and U. Mosel, Z. Phys. A **358**, 357 (1997).  
[59] E. Ya. Paryev, Eur. Phys. J. A **5**, 307 (1999).  
[60] H. Nagahiro, S. Hirenzaki, E. Oset, and A. Ramos, Phys. Lett. B **709**, 87 (2012).  
[61] S. Friedrich *et al.*, CBELSA/TAPS Collaboration, Phys. Lett. B **736**, 26 (2014).  
[62] B. Aubert *et al.*, Phys. Rev. D **70**, 112006 (2004).  
[63] H. Nagahiro *et al.*, Phys. Rev. C **80**, 025205 (2009).  
[64] H. Nagahiro *et al.*, Nucl. Phys. A **761**, 92 (2005).  
[65] H. Nagahiro *et al.*, Phys. Rev. C **87**, 045201 (2013).  
[66] M. Kotulla *et al.*, CBELSA/TAPS Collaboration, Phys. Rev. Lett. **114**, 199903 (2015).  
[67] G. I. Lykasov *et al.*, Eur. Phys. J. A **6**, 71 (1999).  
[68] E. Oset and A. Ramos, Phys. Lett. B **704**, 334 (2012).  
[69] V. Metag, Hyp. Int. **234**, 25 (2015).  
[70] E. Czerwinski *et al.*, Phys. Rev. Lett. **113**, 062004 (2014).  
[71] H. Gilg *et al.*, Phys. Rev. C **62**, 025201 (2000).  
[72] K. Itahashi *et al.*, Phys. Rev. C **62**, 025202 (2000).  
[73] H. Geissel *et al.*, Phys. Rev. Lett. **88**, 122301 (2002).  
[74] K. Suzuki *et al.*, Phys. Rev. Lett. **92**, 072302 (2004).  
[75] P. Kienle and T. Yamazaki, Prog. Part. Nucl. Phys. **52**, 85 (2004).  
[76] E. Marco and W. Weise, Phys. Lett. B **502**, 59 (2001).  
[77] K. Itahashi *et al.*, Prog. Theo. Phys. **128**, 601 (2012).  
[78] N. Muramatsu *et al.*, arXiv:1307.6411.  
[79] V. Metag *et al.*, approved proposal ELSA/3-2012-BGO.